

Kinetically Stabilized Pd@Pt Core–Shell Octahedral Nanoparticles with Thin Pt Layers for Enhanced Catalytic Hydrogenation Performance

Peipei Zhang,^{†,‡,⊥} Yibo Hu,^{†,⊥} Baihai Li,[§] Qiuju Zhang,[†] Chen Zhou,[†] Hongbo Yu,[†] Xuejun Zhang,[‡] Liang Chen,^{*,†} Bryan Eichhorn,^{*,||} and Shenghu Zhou^{*,†}

[†]Ningbo Institute of Materials Technology and Engineering, Chinese Academy of Sciences, 1219 Zhongguan West Road, Ningbo, Zhejiang 315201, People's Republic of China

[‡]College of Applied Chemistry, Shenyang University of Chemical Technology, Shenyang, Liaoning 110142, People's Republic of China

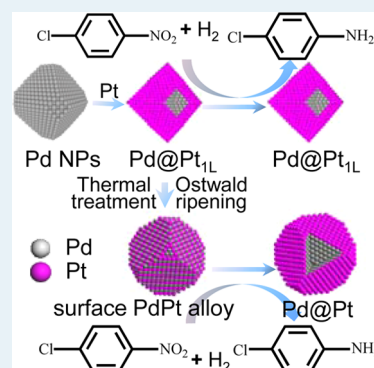
[§]School of Energy Science and Engineering, University of Electronic Science and Technology of China, Chengdu, Sichuan 611731, People's Republic of China

^{||}Department of Chemistry and Biochemistry, University of Maryland, College Park, Maryland 20742, United States

Supporting Information

ABSTRACT: This study investigates the structural stability of small Pd@Pt core@shell octahedral nanoparticles (NPs) and their shell thickness dependent catalytic performance for *p*-chloronitrobenzene hydrogenation with H₂. The 6–8 nm Pd@Pt octahedral NPs are prepared by a sequential reduction method, and the characterization results confirm that Pd@Pt octahedral NPs with one to four atomic Pt layers can be controllably synthesized. The Pd@Pt octahedral NPs with one atomic Pt layer demonstrate excellent structural stability with the maintenance of core–shell structures as well as high catalytic stability during cycle to cycle catalytic *p*-chloronitrobenzene hydrogenation reactions. The alumina-supported Pd@Pt octahedral NPs illustrate a superior catalytic performance relative to individual Pt and Pd and their physical mixtures. Theoretical calculations by density functional theory suggest that the unexpected structural stability for Pd@Pt octahedral NPs with thin Pt shells and their corresponding catalytic stability during hydrogenation reactions can be ascribed to the strong binding between Pt surfaces and reactants/products in catalytic reactions. The enhanced catalytic performance of Pd@Pt octahedral NPs possibly originates from the core–shell interaction, which adjusts the electronic state of surface Pt atoms to be suitable for selective *p*-chloronitrobenzene hydrogenation.

KEYWORDS: Pd@Pt, core–shell, nanocatalysis, hydrogenation, *p*-chloronitrobenzene



1. INTRODUCTION

Bimetallic nanoparticles (NPs) have been applied in many research fields, such as catalysis,^{1–6} electrochemistry,^{7–15} and biological sciences.^{16–19} Among the structures of bimetallic NPs, core@shell NPs have attracted intense interest due to saving precious metals by positioning relatively cheap metals in the cores²⁰ and the performance enhancement by the core–shell interaction.¹⁹ Various core@shell structures have been successfully synthesized, such as Pd@Pt,^{13,21–24} Rh@Pt,²⁵ and Ni@Pt.^{26,27} Ideal core@shell structures are those with just one atomic layer of the shell metal, because the thinnest shell can give the highest shell metal dispersion and the strongest core–shell interaction, thus resulting in the highest specific activity.¹⁹ Although the literature has reported the successful synthesis and application of core–shell structures, the structural stabilities of core@shell NPs have rarely been studied,^{22,28} especially for core–shell structures with thin shells.

The structural stabilities of core@shell NPs are determined by the miscibility of core and shell metals, the shell thickness, and surface–adsorbate interaction during reaction conditions. Pd@Pt bimetallic NPs have been intensely studied due to their enhanced performance in heterogeneous catalysis,²³ hydrogen storage,²¹ and oxygen reduction reactions.^{13,29} However, theoretical analysis and experimental studies indicated the poor structural stability of the Pd@Pt core–shell structure. The difference of cell parameters between Pd and Pt is less than 1.3%, resulting in a PdPt alloy structure at equilibrium. Moreover, because the surface free energy of Pd is lower than that of Pt, the structures with Pd-enriched surfaces are more stable than the Pd@Pt core–shell structure.^{30–32} Furthermore, in hydrogen-related applications, the hydrogen

adsorbate will draw Pd atoms to the topmost surface because of the stronger hydrogen binding on Pd relative to Pt.^{33,34} Therefore, a pure Pt shell on a Pd@Pt NP is difficult to maintain during catalytic hydrogenation reactions, especially for Pd@Pt with one to two atomic Pt layers.

Accordingly, the synthesis of a thermodynamically unstable Pd@Pt core-shell structure is difficult. The Toshima group obtained the inverse Pt@Pd structure by coreduction of PdCl₂ and H₂PtCl₆ by ethanol. The formation of a Pt@Pd core-shell structure is enhanced by the favorable coordination between Pd and the protecting agent—polyvinylpyrrolidone (PVP).³⁵ Some special techniques have been reported in the literature for the synthesis of Pd@Pt core-shell structures. Toshima and co-workers reported a sequential reduction method for synthesis of Pd@Pt core-shell structures using sacrificial hydrogen.²³ Xia and co-workers reported the synthesis of relatively large Pd@Pt nanocubes using a slow injection of Pt precursors to Pd nanocube colloid at a sufficiently high temperature.²²

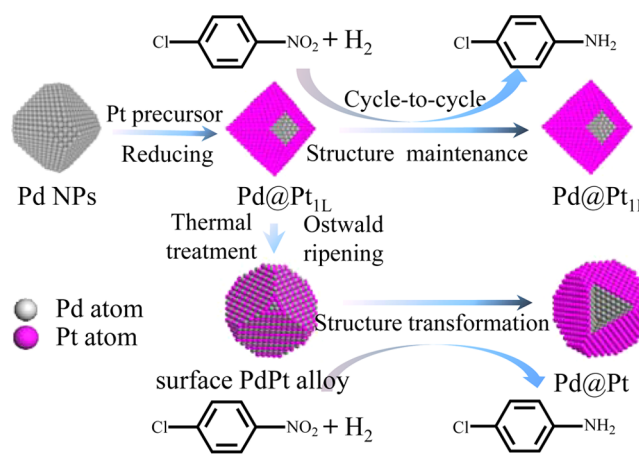
The transformation of Pd@Pt NPs to other more stable structures such as PdPt alloys and Pt@Pd structures has been observed under mild conditions. For example, Crooks and co-workers employed Pd@Cu NPs as precursors in an attempted synthesis of Pd@Pt NPs with one atomic Pt layer (Pd@Pt_{1L}) by galvanic displacement. Surprisingly, they obtained Pt@Pd reverse core-shell structures through the inversion of Pd@Pt structures during the synthetic process at room temperature.³⁶ The Kitagawa group discovered the transformation of Pd@Pt_{2L} NPs to PdPt alloys simply by a process of hydrogen absorption/desorption at 100 °C.²⁸ The above findings confirm the poor structural stability of Pd@Pt core-shell structures with thin Pt shells, consistent with theoretical calculations.

Here, we reported kinetically stabilized small Pd@Pt core-shell NPs with enhanced catalytic performance for *p*-chloronitrobenzene (*p*-CNB) hydrogenation with H₂. The 6–8 nm Pd@Pt octahedral NPs with one to four atomic Pt layers are synthesized by a simple glycol sequential reduction method. The alumina-supported Pd@Pt_{1L} NPs display a superior catalytic performance relative to individual Pd and individual Pt and their physical mixtures. Characterization studies confirm that Pd@Pt core-shell structures are maintained after multiple cycles of catalytic hydrogenation. Moreover, the surface PdPt alloy NPs obtained by thermal treatment of Pd@Pt_{1L} at high temperatures are effectively converted to Pd@Pt core-shell structures after catalytic hydrogenation of *p*-CNB. These findings show that the Pt–adsorbate interaction can not only stabilize the Pd@Pt structure but also induce segregation of Pt to the surface from a PdPt alloy structure during catalytic reactions. Theoretical calculations by density functional theory (DFT) suggest that the superior structural stability of Pd@Pt_{1L} is due to the strong bonding of reactants and products to the Pt surfaces during catalytic reactions. The resultant catalytic performance enhancement possibly originates from the core-shell interaction. A demonstration of kinetically stabilized Pd@Pt NPs during catalytic *p*-CNB hydrogenation is illustrated in Scheme 1.

2. EXPERIMENTAL SECTION

2.1. Chemicals. Palladium chloride (PdCl₂) and ammonium hexachloroplatinate(IV) ((NH₄)₂PtCl₆) were purchased from Aladdin. Polyvinylpyrrolidone (PVP-K30, GR), ethylene glycol (EG, AR), absolute ethyl alcohol (AR), acetone (AR), and *p*-chloronitrobenzene (*p*-CNB, CP) were purchased from Shanghai Chemical Reagent Co.

Scheme 1. Synthesis of Pd@Pt Core-Shell NPs and Their Stabilization during *p*-CNB Hydrogenation Reactions



Aluminum oxide powders were purchased from Qingdao Haiyang Chemical Co., Ltd. All of the reagents were used as received without further purification.

2.2. Syntheses of Individual Pd, Individual Pt, and Pd@Pt Core-Shell NPs and Alumina-Supported Nanocatalysts.

2.2.1. Synthesis of Individual Pd NPs. In a typical synthesis, 0.352 mmol of PdCl₂, 120.0 mg of PVP-K30, and 25.0 mL of EG were transferred into a 50 mL three-necked round-bottom flask, and the resultant mixture was heated and maintained at 60 °C for 30 min with magnetic stirring under an N₂ atmosphere. The mixture was then heated and maintained at 90 °C for 30 min, and then the dark solution was further heated and maintained at 150 °C for 2 h. The resultant solution was cooled to room temperature, followed by centrifugation with acetone. The obtained black powdery product was then redispersed in ethyl alcohol for future use.

2.2.2. Synthesis of Individual Pt NPs. The synthesis of Pt NPs was similar to that of Pd NPs. In a typical synthesis, 0.352 mmol of (NH₄)₂PtCl₆, 120.0 mg of PVP-K30, and 25.0 mL of EG were transferred into a 50 mL three-necked round-bottom flask, and the resultant mixture was heated and maintained at 90 °C for 30 min with magnetic stirring under an N₂ atmosphere. The mixture was then heated and maintained at 130 °C for 30 min. The solution was further heated and maintained at 150 °C for 2 h. The Pt NP collection process is similar to that for Pd NPs.

2.2.3. Synthesis of Pd@Pt Core-Shell NPs. Various Pd@Pt NPs with different Pd/Pt ratios were synthesized by a sequential reduction method. For the synthesis of Pd@Pt NPs with a 1/1 Pd/Pt ratio, 10.0 g of the aforementioned as-synthesized Pd colloid containing 0.126 mmol of Pd, 10.0 mL of EG, 0.126 mmol of (NH₄)₂PtCl₆, and 30.0 mg of PVP-K30 were mixed in a 50 mL three-necked round-bottom flask with magnetic stirring under an N₂ atmosphere. The resultant mixture was heated and maintained at 90 °C for 30 min. The solution was then heated and maintained at 130 °C for 30 min to reduce the Pt precursors and then heated and maintained at 150 °C for 2 h. The Pd@Pt nanoparticle collection process is similar to that for Pd NPs. The Pd@Pt core-shell NPs with Pd/Pt ratios of 1/0.75, 1/0.5, 1/0.25, and 1/0.125 were synthesized by a similar method through adjustment of the amount of Pt precursors, and the other conditions were same as those of Pd@Pt NPs at a Pd/Pt ratio of 1/1. The Pd@Pt NPs with Pd/Pt ratios of 1/1, 1/0.75, 1/0.5, 1/0.25, and 1/0.125 are denoted as Pd@Pt-1/1, Pd@Pt-1/0.75, Pd@Pt-1/0.5, Pd@Pt-1/0.25, and Pd@Pt-1/0.125, respectively.

2.2.4. Synthesis of Al₂O₃-Supported Nanocatalysts. A defined amount of the aforementioned as-synthesized colloid was centrifuged once with acetone, and the obtained black powdery product was redispersed in 30.0 mL of ethanol. The resultant colloid was transferred into a 50 mL three-necked round-bottom flask, and 1.0 g of Al₂O₃ calcined at 550 °C for 2 h (specific surface area 185 m²/g) was then added to the colloid. The resultant mixture was heated with

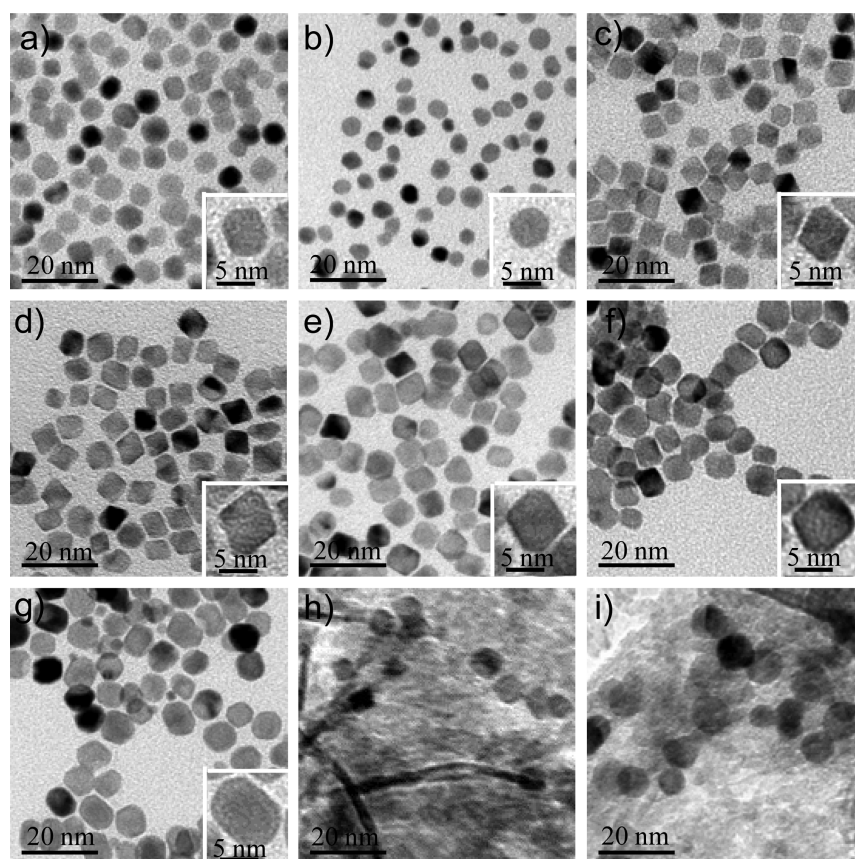


Figure 1. TEM images showing (a) Pd, (b) Pt, (c) Pd@Pt-1/0.125, (d) Pd@Pt-1/0.25, (e) Pd@Pt-1/0.5, (f) Pd@Pt-1/0.75, (g) Pd@Pt-1/1, and (h) Pd@Pt-1/0.25/Al₂O₃ after five cycles of catalytic p-CNB hydrogenation reactions at 45 °C and ambient H₂ pressure and (i) Pd@Pt-1/0.25/Al₂O₃ after catalytic p-CNB hydrogenation reactions at 200 °C and 4.0 MPa of H₂. The inserts show enlarged TEM images of individual nanoparticles. Scale bars in (a)–(i) are 20 nm; scale bars in the insets are 5 nm.

magnetic stirring at 60 °C and purged with N₂ to remove the ethanol. The resultant gray powdery solid was further heated at 60 °C in an oven overnight. The product was then washed one time with acetone and four times with ethanol to thoroughly remove surfactants, followed by drying in an oven at 60 °C overnight to give Al₂O₃-supported nanocatalysts.

2.3. Characterization. Transmission electron microscopy (TEM) images were obtained by using a JEOL 2100 transmission electron microscope operated at 200 kV. The high angle annular dark field scanning transition electron microscopy (HAADF-STEM) images, phase mapping, and line scans by energy-dispersive spectroscopy (EDS) were obtained using a TitanG2 80-200 ChemiSTEM equipped with a Super-X EDX detector system Cs-corrected STEM. X-ray photoelectron spectra (XPS) were taken on AXIS ULTRA DLD multifunctional X-ray photoelectron spectroscope with an Al source. The data processing was performed using CasaXPS software. The contents of Pt and Pd in the supernatant solution after centrifugation were determined with a PE Optima 2100DV inductive coupled plasma optical emission spectrometer (ICP-OES). The diffuse reflectance Fourier transform infrared spectra (DRIFT-IR) with CO probes were obtained using a Nicolet-6700 Fourier transform infrared spectrometer. The alumina-supported nanocatalysts were pretreated with H₂ at 100 °C for 30 min at a gas flow rate of 20 mL/min and subsequently purged with Ar at 100 °C for 20 min. The samples were then cooled to 30 °C and recorded as the DRIFT-IR background spectrum. The alumina-supported nanocatalysts were further treated with pure CO (99.99%) at a gas flow rate of 20 mL/min at 30 °C for 30 min and subsequently purged with Ar to remove the free CO before the DRIFT-IR spectra were recorded.

2.4. Catalytic p-CNB Hydrogenation with H₂. **2.4.1. Hydrogenation of p-CNB with H₂ at Ambient Pressure.** A 100 mL three-necked round-bottom flask was filled with 0.100 g of alumina-

supported nanocatalysts, 50.0 mL of absolute ethanol, and 3.0 g of p-CNB. The mixture was heated and maintained at 45 °C with vigorous stirring. The reaction system was kept under an H₂ atmosphere with a hydrogen flow for the defined reaction time. The liquid products were analyzed by a gas chromatograph equipped with a flame ionization detector. For cycle to cycle catalytic reactions, the catalysts were collected after catalytic reactions by centrifugation with ethyl alcohol and drying in an oven at 60 °C overnight. Because some of the supported catalysts were lost during the recovery process, in the subsequent cycle reactions, proportional amounts of p-CNB and absolute ethanol were used to keep the p-CNB/catalyst and p-CNB/solvent ratios the same as those of the first catalytic run.

2.4.2. Hydrogenation of p-CNB with H₂ at the H₂ Partial Pressure of 4.0 MPa. Typically, a 500 mL high-pressure agitated autoclave was filled with 0.200 g of alumina-supported nanocatalysts, 200 mL of absolute ethanol, and 12.0 g of p-CNB. The autoclave was then purged with hydrogen at least three times at room temperature. The hydrogenation reactions were carried out at 200 °C and a hydrogen partial pressure of 4.0 MPa with a stirring rate of 500 rpm for 3 h.

3. RESULTS AND DISCUSSION

3.1. Synthesis and Characterization of Pd@Pt Core–Shell NPs. Pd@Pt octahedral NPs were synthesized by a simple sequential reduction method. Pd NPs were first prepared by reduction of Pd precursors by glycol using PVP as the capping agent. Pt was further deposited on the Pd seeds to form core@shell structures. The ICP-OES study suggests that greater than 99.5% of the Pd and Pt in the starting materials is reduced to form NPs.

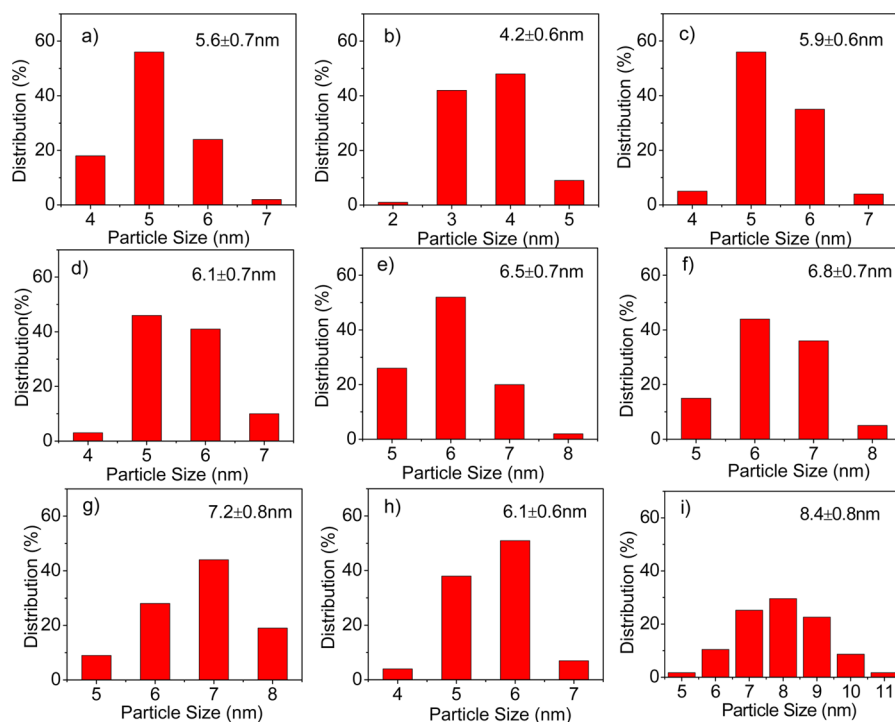


Figure 2. Size analyses of individual and core-shell NPs showing (a) Pd, (b) Pt, (c) Pd@Pt-1/0.125, (d) Pd@Pt-1/0.25, (e) Pd@Pt-1/0.5, (f) Pd@Pt-1/0.75, (g) Pd@Pt-1/1, and (h) Pd@Pt-1/0.25 after five cycles of catalytic p-CNB hydrogenation reactions at 45 °C and ambient H₂ pressure and (i) Pd@Pt-1/0.25/Al₂O₃ after catalytic p-CNB hydrogenation reactions at 200 °C and 4.0 MPa of H₂.

TEM images of Pd@Pt are shown in Figure 1, and their corresponding size analyses are shown in Figure 2. Pd NPs in Figure 1a show well-faceted shapes with an average particle size of 5.6 nm, while Pt NPs in Figure 1b are relatively spherical with an average particle size of 4.2 nm. Pd@Pt NPs with Pt/Pd ratios of 0.125/1, 0.25/1 and 0.5/1 are illustrated in Figure 1c–e, respectively, and octahedral shapes are observed for those NPs. The octahedral shapes with sharp corners are evidenced by the insets of Figure 1c–e and are consistent with the literature.³⁷ In contrast, at higher Pt/Pd ratios of 0.75/1 in Figure 1f and 1/1 in Figure 1g, the Pd@Pt NPs contain octahedral shapes with some other shapes, indicating that the influence of Pd seeds on the shape of Pt shells decreases at higher Pt/Pd ratios. Size analyses of Pd@Pt NPs in Figure 2c–g show a continuous increase in particle size from 5.9 to 7.2 nm when the Pt/Pd ratios increase from 0.125/1 to 1/1, indicating the continuous Pt deposition on Pd nanoparticle surfaces.

XPS spectra of Pd@Pt with different Pt/Pd ratios are illustrated in Figure S1 in the Supporting Information. The XPS curve fitting employs the method of Doniach and Sunjic,³⁸ and the binding energy assignment is according to the literature.^{36,39,40} Table 1 summarizes the Pt/Pd atomic ratios for Pd@Pt NPs by XPS. Approximately 3.5–6.1 atomic % of Pd^{δ+} and Pt²⁺ species are observed for Pd@Pt NPs, presumably due to the colloid exposure to air. The Pt/Pd ratio for the Pd@Pt-

1/1 NPs by EDS is 1.02/1.00, which is close to the 1/1 Pt/Pd ratio in the starting materials. However, the Pt/Pd ratio for the Pd@Pt-1/1 NPs obtained by XPS is 3.13/1.00, which is significantly higher than that obtained by EDS. The same phenomenon is also observed for the Pd@Pt-1/0.5 and Pd@Pt-1/0.25 NPs, which show 2 times higher Pt/Pd ratios by XPS in comparison to those found by EDS. Since XPS is a surface-sensitive technique, these data reveal compositions of the outer layers for core@shell NPs. Therefore, the higher Pt/Pd ratios by XPS are consistent with the core@shell structure with Pd cores and Pt shells.

The relative atomic concentrations of Pd and Pt by line scans and elemental phase mapping by EDS for Pd@Pt NPs are shown in Figure 3. The HAADF-STEM images and relative atomic concentrations of Pd and Pt by the EDS line scans for Pd@Pt-1/0.25 are shown in Figure 3a,b, respectively. The highest Pd concentration is found at the center of Pd@Pt particles, while the highest Pt concentration is found at the peripheries of particles, suggesting a core@shell structure with Pd cores and Pt shells. The Pd cores and very thin Pt shells are clearly observed in the combined Pd and Pt phase mapping in Figure 3f. The HAADF-STEM images and relative atomic concentrations of Pd and Pt by the EDS line scans for Pd@Pt-1/1 are shown in Figure 3g,h, respectively. The highest Pt atomic concentration at the peripheries of NPs is more clearly observed in Figure 3h in comparison to that of Pd@Pt-1/0.25 in Figure 3b due to the thicker Pt shells at a higher Pt/Pd ratio of 1/1 in the Pd@Pt-1/1 NPs. The thicker Pt shells are also confirmed by the combined phase mapping of Pd and Pt for the Pd@Pt-1/1 NPs in Figure 3l.

DRIFT-IR spectra with CO probes of alumina-supported Pd, Pt, and Pd@Pt NPs with different Pt/Pd ratios are shown in Figure 4. As shown in Figure 4a, Pd/Al₂O₃ exhibits a band at 1946 cm⁻¹, which is a characteristic band of bridged CO on Pd

Table 1. Pt/Pd Atomic Ratios with Different Oxidation States from the XPS Analysis for Pd@Pt Core-Shell NPs

sample	Pd ⁰ /Pd ^{δ+}	Pt ⁰ /Pt ²⁺	Pt/Pd (XPS)	Pt/Pd (EDS)
Pd@Pt-1/1	96.4/3.6	96.5/3.5	3.13/1.00	1.02/1.00
Pd@Pt-1/0.5	95.0/5.0	96.0/4.0	1.15/1.00	0.52/1.00
Pd@Pt-1/0.25	93.9/6.1	94.0/6.0	0.52/1.00	0.26/1.00

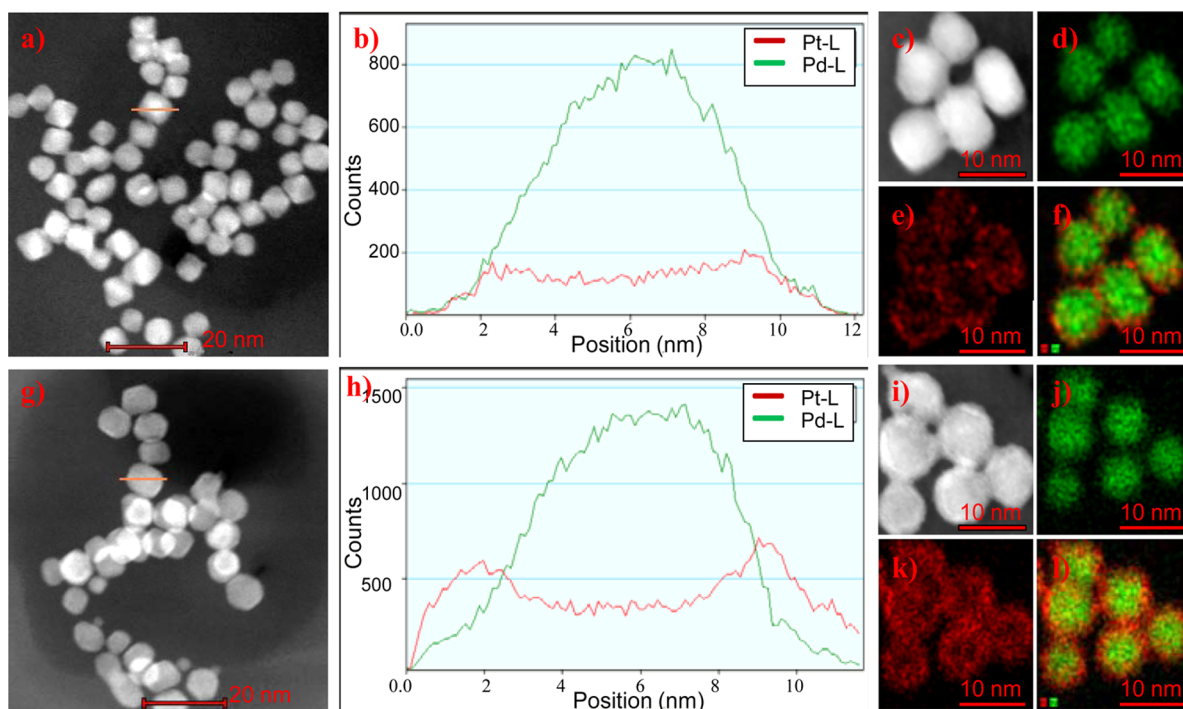


Figure 3. (a)–(f) EDS line scans and phase mapping for Pd@Pt-1/0.25 NPs: (a) HAADF-STEM image (the particle with a yellow line is for the EDS line scan); (b) relative atomic concentrations of Pd and Pt by EDS line scans; (c) selected area for EDS phase mapping; (d) Pd phase mapping; (e) Pt phase mapping; (f) the combined Pd and Pt phase mapping. (g)–(l) HAADF-STEM image, relative atomic concentrations of Pd and Pt by EDS line scans, selected area for EDS phase mapping, Pd phase mapping, Pt phase mapping, and the combined Pd and Pt phase mapping for Pd@Pt-1/1, respectively. Scale bars in (a) and (g) are 20 nm; scale bars in (c)–(f) and (i)–(l) are 10 nm.

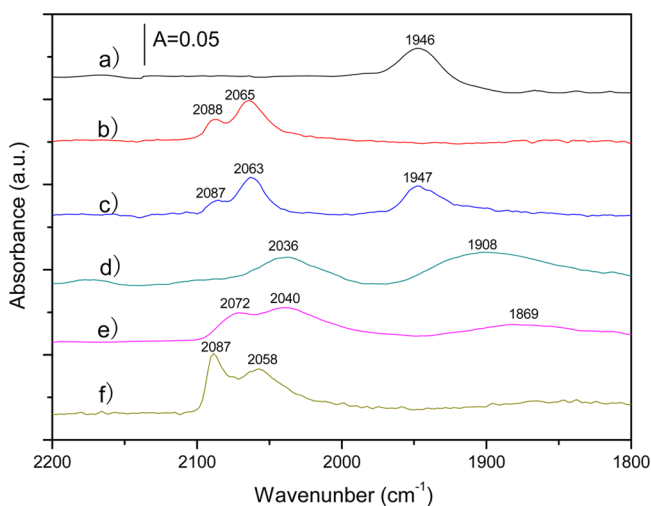


Figure 4. DRIFT-IR spectra with CO probes showing (a) Pd/Al₂O₃, (b) Pt/Al₂O₃, (c) the physical mixture of Pd/Al₂O₃ and Pt/Al₂O₃ with a Pt/Pd ratio of 1/1, (d) Pd@Pt-1/0.125/Al₂O₃, (e) Pd@Pt-1/0.25/Al₂O₃, and (f) Pd@Pt-1/1/Al₂O₃.

sites.^{41–44} The band near 2100 cm⁻¹ for linear CO on Pd sites is not observed for Pd/Al₂O₃, which is consistent with the reported spectra of well-faceted Pd NPs.⁴⁴ Figure 4b shows the DRIFT-IR spectrum of alumina-supported Pt NPs. Two characteristic bands at 2065 and 2088 cm⁻¹ are clearly observed, and the former is ascribed to linear CO on Pt step and kink sites, and the latter can be attributed to linear CO on Pt terrace sites.^{23,24,45} A 1860 cm⁻¹ band for bridged CO on Pt sites is not observed for these particles,²⁴ indicating a low concentration of bridged CO.^{46,47} The DRIFT-IR spectrum of

alumina-supported physical mixtures of Pd and Pt NPs is shown in Figure 4c. The bands at 2087 and 2063 cm⁻¹ for linear CO on Pt sites and 1947 cm⁻¹ for bridged CO on Pd sites are observed, consistent with the spectrum of the physical mixture of Pd and Pt NPs.

DRIFT-IR spectra of Pd@Pt/Al₂O₃ with different Pt/Pd ratios are shown in Figure 4d–f. The alumina-supported Pd@Pt-1/0.125 nanocatalyst shown in Figure 4d exhibits bands at 2036 and 1908 cm⁻¹, where the former is assigned to linear CO on Pt sites and the latter is ascribed to bridged CO on Pd sites. The copresence of CO binding on Pt and Pd sites is consistent with an incomplete Pt coverage on the Pd seeds at a low Pt/Pd ratio of 0.125/1. When the Pt/Pd ratio is increased to 0.25/1 (Figure 4e), a slight hump at 1869 cm⁻¹ for bridged CO on Pt sites and bands at 2040 and 2072 cm⁻¹ for linear CO on Pt sites are present while the bands around 1950 cm⁻¹ for bridged CO on Pd sites are absent, indicating a complete Pt coverage on the Pd seeds at a Pt/Pd ratio of 0.25/1. Similarly, the spectrum of supported Pd@Pt-1/1 NPs in Figure 4f only shows CO absorption on the Pt surface (2087 and 2058 cm⁻¹), further confirming a core@shell structure.

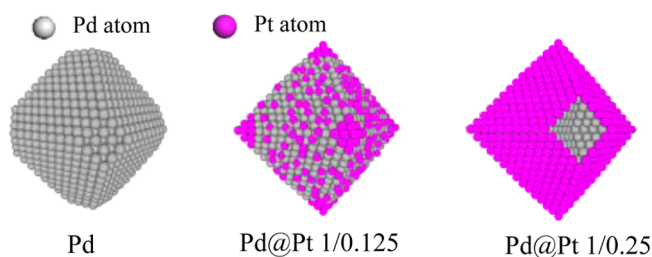
The individual Pt NPs exhibit two characteristic bands at 2065 and 2088 cm⁻¹. In contrast, the Pd@Pt-1/0.25 NPs with a full Pt coverage illustrate two linear CO absorption bands at 2040 and 2072 cm⁻¹ with one band at 1869 cm⁻¹ for bridged CO. When the Pt/Pd ratio increases to 1/1, the Pd@Pt-1/1 NPs show CO absorption bands at 2058 and 2087 cm⁻¹, which is very similar to those of individual Pt NPs, indicating that the influence of Pd cores decreases with an increase in the thickness of Pt shells. For the Pd@Pt-1/0.125 NPs with an incomplete Pt coverage, the bands for the linear CO on Pt sites merge into one band at 2036 cm⁻¹ for linear CO on Pt step and kink sites.

The presence of only linear CO binding on Pt step and kink sites is consistent with the presence of mostly isolated Pt atoms at a low Pt/Pd ratio of 0.125/1.

According to the diameter of the Pt atom and close-packed model of Pt on Pd seeds, one complete Pt atomic layer accounts for 0.45 nm.³⁶ From these structural models, the particle size of a Pd@Pt NP with one complete atomic Pt layer (Pd@Pt_{1L}) using 5.6 nm Pd seeds should be 6.1 nm while the particle sizes of Pd@Pt_{2L} and Pd@Pt_{3L} are 6.5 and 7.0 nm, respectively. Actually, the measured particle size of the Pd@Pt-1/0.25, Pd@Pt-1/0.5, and Pd@Pt-1/1 NPs are 6.1, 6.5, and 7.2 nm, respectively, which is consistent with the Pd@Pt_{1L}, Pd@Pt_{2L}, and Pd@Pt_{3-4L} assignments, respectively. It can be concluded that Pd@Pt NPs have a core-shell structure with Pd cores and Pt shells, and the thickness of Pt shell can be well controlled by the current method. At a Pt/Pd ratio of 0.25/1, Pd@Pt-1/0.25 is in line with the Pd@Pt_{1L} structure.

Xia and co-workers has reported a growth model from Pd cubes to Pd octahedra through the Pd cuboctahedron intermediate.³⁷ In this study, the Pd seeds are cuboctahedra in Figure 1a, and the Pd@Pt core-shell NPs are octahedra in Figure 1c-e, which is quite consistent with a growth model from Pd cuboctahedra to Pd@Pt octahedra. The schematic demonstration of the formation of Pd@Pt core-shell octahedral NPs is shown in Scheme 2.

Scheme 2. Schematic Demonstration of the Formation of Pd@Pt Core-Shell Octahedral NPs with One Pt Atomic Layer from Pd Cuboctahedral NP Seeds



3.2. Catalytic p-CNB Hydrogenation over Supported Pd@Pt NPs. Catalytic p-CNB hydrogenation with H₂ was used to investigate the catalytic performance of alumina-supported Pd@Pt NPs. As for p-CNB hydrogenation, the major product is *p*-chloroaniline (p-CAN) with aniline (AN) and 4-aminophenol (4-AP) as byproducts from dechlorination reactions.⁴⁸⁻⁵¹

The catalytic performances of p-CNB hydrogenation over supported nanocatalysts at ambient H₂ pressure and 45 °C are shown in Table 2. The Pt/Al₂O₃ catalysts illustrate 79.5% of p-CNB conversion and 81.5% of p-CAN selectivity, while Pd/Al₂O₃ catalysts show 61.7% of conversion and 45.8% of p-CAN selectivity. For the Pd@Pt-1/0.125/Al₂O₃ catalysts, p-CNB conversion and p-CAN selectivity are between those of supported Pd and Pt nanocatalysts. In contrast, the Pd@Pt-1/0.25/Al₂O₃ catalysts illustrate 98.5% of conversion and 82.1% of p-CAN selectivity, showing a better performance than Pd/Al₂O₃, Pt/Al₂O₃, and their physical mixture (Pd+Pt)-1/0.25/Al₂O₃. With continuously increasing Pt/Pd ratios, Pd@Pt-1/0.5/Al₂O₃, Pd@Pt-1/0.75/Al₂O₃, and Pd@Pt-1/1/Al₂O₃ show decreased conversions with enhanced p-CAN selectivity. Pd@Pt-1/0.25/Al₂O₃ was also selected for hydrogenation at critical conditions and shows enhanced p-CNB conversion and p-CAN

Table 2. Catalytic Performance of p-CNB Hydrogenation with H₂ over Supported Individual and Core@Shell Nanocatalysts^a

catalyst	conversion (%)	selectivity (%)			
		p-CAN	AN	4-AP	other
Pt/Al ₂ O ₃	79.5	81.5	12.4	2.4	3.7
Pd/Al ₂ O ₃	61.7	45.8	43.0	9.3	1.9
(Pd+Pt)-1/0.25/Al ₂ O ₃	74.3	60.9	29.2	5.2	4.7
Pd@Pt-1/0.125/Al ₂ O ₃	70.7	69.8	14.7	11.4	4.1
Pd@Pt-1/0.25/Al ₂ O ₃	98.5	82.1	10.4	7.1	0.4
Pd@Pt-1/0.5/Al ₂ O ₃	97.4	87.9	9.5	2.6	0.0
Pd@Pt-1/0.75/Al ₂ O ₃	91.2	86.3	11.4	2.3	0.0
Pd@Pt-1/1/Al ₂ O ₃	88.0	86.9	11.0	2.1	0.0

^aReaction conditions: p-CNB, 2.0 g; supported catalysts, 0.100 g; EtOH, 50 mL; 0.10 MPa H₂; reaction temperature, 45 °C; reaction time, 3.0 h; speed of agitation, 500 rpm; Pd/Al₂O₃ (Pd loading 0.54 wt %); Pt/Al₂O₃ (Pt loading 1.00 wt %); physical mixture and core@shell catalysts (fixed Pd loading 0.54 wt %, Pt loading changed with the Pt/Pd molar ratio).

selectivity at higher temperatures and higher H₂ pressure (see Table S1 in the Supporting Information). The effects of reaction temperatures and reaction time on the catalytic performance over Pd@Pt-1/0.25/Al₂O₃ are shown in Figures S2 and S3 in the Supporting Information. Basically, with an increase in reaction temperatures and reaction times, the p-CNB conversion and p-CAN selectivity are increased, and at a reaction time of 3.0 h and reaction temperature of 45 °C, the p-CNB conversion and p-CAN selectivity over Pd@Pt-1/0.25/Al₂O₃ reach 98.5% and 82.1%, respectively.

The Pd@Pt/Al₂O₃ nanocatalysts illustrate a Pt shell thickness dependent catalytic performance for p-CNB hydrogenation. The Pd@Pt-1/0.125/Al₂O₃ catalysts with an incomplete Pt shell show catalytic performance between those of Pd and Pt nanocatalysts, which is consistent with the structure of an incomplete Pt shell and some naked Pd surfaces. The Pd@Pt-1/0.25/Al₂O₃ catalysts (Pd@Pt_{1L}/Al₂O₃) illustrate a significantly enhanced p-CNB conversion with slightly enhanced p-CAN selectivity, showing the advantage of the core@shell structure for catalytic reactions. The Pd@Pt-1/0.5/Al₂O₃ catalysts (Pd@Pt_{2L}/Al₂O₃) demonstrate the best catalytic performance with 97.4% of conversion and 87.9% of p-CAN selectivity, indicating the most suitable core-shell interaction obtained at the Pt/Pd ratio of 0.5/1 for catalytic p-CNB hydrogenation. When the thickness of the Pt shell of Pd@Pt NPs continuously increases, the conversions over Pd@Pt-1/0.75/Al₂O₃ and Pd@Pt-1/1/Al₂O₃ catalysts decrease, which suggests a decreased core-shell interaction at higher Pt/Pd ratios.

3.3. Structural and Catalytic Stability of Pd@Pt NPs with One Atomic Pt Layer. The Pd@Pt_{1L}/Al₂O₃ nanocatalysts (Pd@Pt-1/0.25/Al₂O₃) were selected to study the catalytic stability of Pd@Pt nanocatalysts. Table 3 illustrates the results of cycle to cycle p-CNB hydrogenation reactions over Pd@Pt_{1L}/Al₂O₃. From cycle 1 to cycle 5, the p-CNB conversion over Pd@Pt-1/0.25/Al₂O₃ is highly stable while p-CAN selectivity increases from 82.5% in cycle 1 to 89.3% in cycle 2 and is stable in the following cycles. In this study, the amounts of p-CNB and solvent decrease according to the weight of the used catalysts recovered from each cycle, and no fresh catalysts are added into the system. Due to the loss in the

Table 3. Cycle to Cycle p-CNB Hydrogenation Reaction over Pd@Pt_{IL}/Al₂O₃

cycle index ^a	amt of catalyst (g)	amt of p-CNB (g)	conversion (%)	p-CAN selectivity (%)
1	0.100	2.00	98.4	82.5
2	0.077	1.55	99.6	89.3
3	0.069	1.38	98.5	89.5
4	0.055	1.10	98.7	87.2
5	0.047	0.93	99.2	90.6

^aReaction conditions: Pd@Pt-1/0.25/Al₂O₃; EtOH in cycle 1, 50.0 mL; EtOH in the following cycles decreased according to the weight of p-CNB at a fixed EtOH/p-CNB ratio; 0.10 MPa of H₂; reaction time, 3.0 h; reaction temperature, 45 °C; agitation speed, 500 rpm.

catalyst recovery process, five cycles of catalytic p-CNB hydrogenation reactions were carried out. This study strongly suggests that Pd@Pt_{IL} is catalytically stable for cycle to cycle p-CNB hydrogenation with H₂.

A DRIFT-IR study with CO probes was carried out to study the structural stability of Pd@Pt_{IL} NPs after catalytic reactions. Figure 5 illustrates DRIFT-IR spectra of the Pd@Pt-1/0.25/

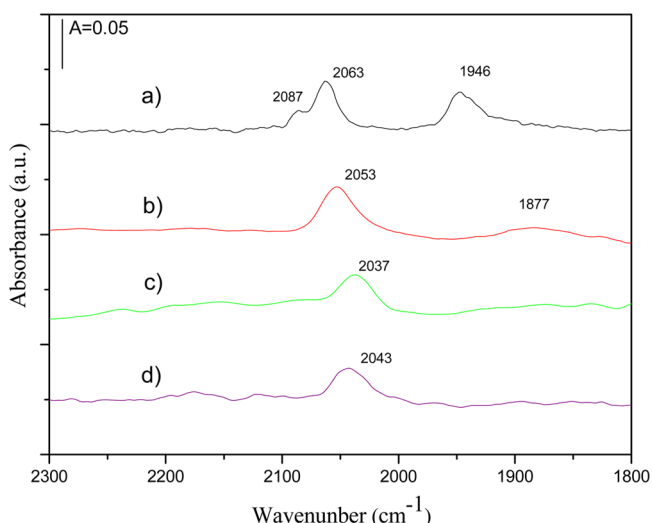


Figure 5. DRIFT-IR spectra with CO probes showing (a) the physical mixture of Pd/Al₂O₃ and Pt/Al₂O₃ with a 1/1 Pt/Pd ratio, (b) Pd@Pt-1/0.25/Al₂O₃ after five cycles of p-CNB hydrogenation at ambient H₂ pressure and 45 °C, (c) Pd@Pt-1/0.25/Al₂O₃ after p-CNB hydrogenation at 4.0 MPa H₂ and 200 °C, and (d) Pd@Pt-1/0.25/Al₂O₃ after p-CNB hydrogenation at 4.0 MPa H₂ and 250 °C.

Al₂O₃ nanocatalysts after catalytic reactions. As shown in Figure 5b, the DRIFT-IR spectrum of Pd@Pt-1/0.25/Al₂O₃ after five cycles of hydrogenation reactions at 45 °C and ambient H₂ pressure only shows the linear CO band on Pt sites at 2053 cm⁻¹ and bridged CO band on Pt sites at 1877 cm⁻¹, confirming the maintenance of the core@shell structure during cycle to cycle reactions. In comparison with the spectrum of as-prepared Pd@Pt-1/0.25/Al₂O₃ in Figure 4e, the linear CO band at 2072 cm⁻¹ disappears, suggesting the occurrence of surface reconstruction during catalytic reactions.

The Pd@Pt_{IL}/Al₂O₃ catalysts also demonstrate structural stability during catalytic p-CNB hydrogenation under critical reaction conditions. As shown in Figure 5c, the Pd@Pt-1/0.25/Al₂O₃ catalysts after catalytic reactions at 200 °C and 4.0 MPa of H₂ only exhibit a linear CO band on Pt sites at 2037 cm⁻¹ with the absence of the band for CO binding on Pd sites, confirming the maintenance of core@shell structures during catalytic hydrogenation under critical reaction conditions. For catalytic hydrogenation at an even higher reaction temperature of 250 °C and 4.0 MPa of H₂, although byproduct formation is more severe at 250 °C than that at 200 °C (Table S1 in the Supporting Information), the Pd@Pt-1/0.25 nanocatalysts still maintain a core@shell structure, as evidenced by the presence of only a linear CO band on Pt sites at 2043 cm⁻¹ in Figure 5d.

The EDS line scans and phase mapping of the Pd@Pt_{IL}/Al₂O₃ catalysts used are shown in Figure 6. As illustrated in Figure 6, the core-shell structure with Pd cores and Pt shells is clearly observed for the Pd@Pt-1/0.25/Al₂O₃ after five cycles of catalytic p-CNB hydrogenation at 45 °C and ambient H₂ pressure, which is consistent with the DRIFT-IR result in Figure 5b. Moreover, the TEM images of Pd@Pt-1/0.25/Al₂O₃ after cycle to cycle reactions in Figure 1h and size analysis in Figure 2h suggest that Pd@Pt-1/0.25 maintained the same octahedral shapes and nearly the same average size of Pd@Pt NPs in comparison to those of as-prepared Pd@Pt-1/0.25 NPs, further confirming the structural stability of Pd@Pt_{IL} NPs after cycle to cycle reactions. The phase mapping of supported Pd@Pt-1/0.25 after catalytic reaction at 200 °C and 4.0 MPa of H₂ is shown in Figure S4 in the Supporting Information. Due to the Ostwald ripening process during high-temperature catalytic reaction, the particle size increases (Figures 1i and 2i), but the phase mapping still clearly demonstrates that the Pt atoms are mainly on the surfaces of NPs, which is consistent with the DRIFT-IR result in Figure 5c. The maintenance of a pure Pt shell in the presence of Ostwald ripening in high-temperature catalytic reactions suggests that some factors during the

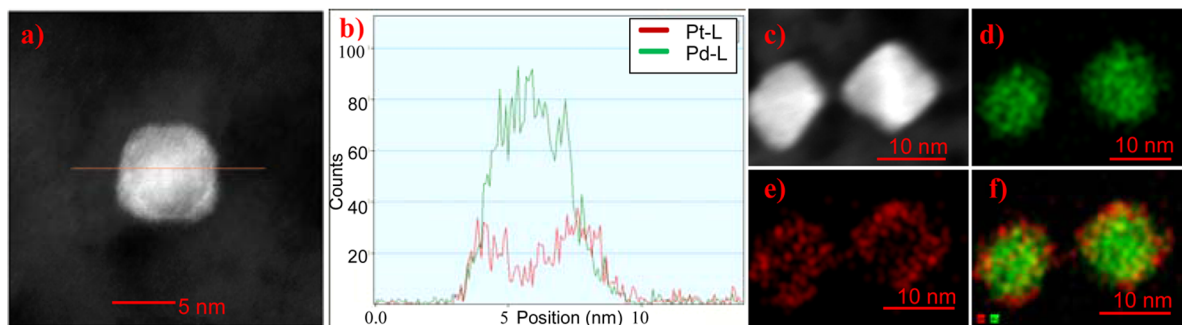


Figure 6. EDS line scans and phase mapping for Pd@Pt-1/0.25/Al₂O₃ after five cycles of p-CNB hydrogenation: (a) HAADF-STEM image of selected particles for line scans; (b) relative concentrations of Pd and Pt by EDS line scans; (c) selected area for phase mapping; (d) Pd phase mapping; (e) Pt phase mapping; (f) combined Pd and Pt phase mapping. The scale bar in (a) is 5 nm; scale bars in (c)–(f) are 10 nm.

catalytic reaction help to keep the Pt surface, and this will be discussed later.

The thermal stability of Pd@Pt_{1L}/Al₂O₃ under an Ar and H₂ atmosphere was also studied, and their corresponding DRIFT-IR spectra are shown in Figure S5 in the Supporting Information. Pd@Pt_{1L}/Al₂O₃ after H₂ treatment at 4.0 MPa and 250 °C exhibits CO absorption bands for Pt sites as well as Pd sites, suggesting the transformation of Pd@Pt core-shell structures to the surface PdPt alloy structure. Moreover, at an even higher temperature of 550 °C, the Ar or H₂ treatment can fully transform the Pd@Pt core-shell structure into a structure with a pure Pd surface, as evidenced by the sole presence of CO absorption bands for Pd sites.

3.4. Discussion of the Structural Stability and Core-Shell Interaction of Pd@Pt/Al₂O₃ NPs. According to the theoretical analysis and experimental data,^{28,36,52} Pd@Pt NPs with a thin Pt layer should only exist at low temperatures and low hydrogen pressures. However, in this study, the Pd@Pt_{1L} NPs are quite stable during catalytic hydrogenation reactions. It is speculated that the p-CNB reactant and p-CAN product in catalytic hydrogenation bond to Pt more strongly relative to Pd, and the stronger bonding stabilizes the Pt topmost surface.

Theoretical calculations by DFT theory was carried out to prove the stronger binding between Pt surfaces and reactants/products (see Figure S6 and Table S2 in the Supporting Information). The binding energy of p-CNB on the Pt(111) surface is -4.56 eV, while that on the Pd(111) surface is -3.28 eV. Moreover, the binding energies of p-CAN on the Pt(111) and Pd(111) surfaces are -4.80 and -4.40 eV, respectively. Apparently, p-CNB and p-CAN bond to the Pt(111) surface more strongly than they bond to Pd(111) surfaces. The stronger bonding of p-CNB and p-CAN to Pt surfaces found by theoretical calculations strongly supports that the energy favorable bindings of reactants and products on Pt sites keep the Pt atoms on the surface layer for Pd@Pt NPs during catalytic reactions.

The experimental data also support that the reactants and products in catalytic p-CNB hydrogenation could stabilize the Pt surfaces of Pd@Pt. As shown in Figure S5e,f in the Supporting Information, the surface PdPt alloy structures obtained by thermal treatment of Pd@Pt_{1L}/Al₂O₃ transforms into Pd@Pt core-shell structures by further catalytic p-chloronitrobenzene hydrogenation at 100 °C and 1.0 MPa of H₂. The above experiments strongly suggest that the reactants and products during catalytic p-CNB hydrogenation not only stabilize the Pt surface of Pd@Pt core-shell NPs but can also induce segregation of Pt atoms to the surfaces from PdPt alloy structures at relatively high temperatures and H₂ pressures.

The catalytic performance of the Pd@Pt_{1L} core-shell structure is superior to that of Pd, Pt, and the physical mixture of Pd and Pt and is highly stable during cycle to cycle hydrogenation reactions. The superior catalytic stability obviously originates from the superior structural stability. In this study, the amount of surface Pt atoms increases with an increase in the Pt/Pd ratios, since the Pd loadings are fixed in all core-shell catalysts. It can be concluded that Pd@Pt_{1L}/Al₂O₃ gives the highest specific activity among core-shell catalysts with full Pt coverage. Considering the nearly same amounts of surface Pt atoms of Pd@Pt_{1L} (Pd@Pt-1/0.25, surface Pt loading 0.25 wt %) and individual Pt (4.2 nm, surface Pt loading 0.26 wt %) according to the theoretical model,⁵³ the enhanced catalytic performance for catalytic p-CNB hydrogenation is ascribed to the core-shell interaction, which adjusts

the electronic state of the surface Pt atoms of Pd@Pt core-shell NPs to be suitable for selective p-chloronitrobenzene hydrogenation. At the same time, the hydrogen adsorption is not decreased due to the favorable hydrogen adsorption on the Pd subsurface layer, since hydrogen adsorption on Pd is a more energy favorable process than hydrogen adsorption on Pt,²¹ thus resulting in an enhanced catalytic performance.

4. CONCLUSIONS

The Pd@Pt core-shell structures are synthesized by a simple sequential glycol reduction method. The characterization reveals that the Pd@Pt NPs with one to four Pt atomic layers can be controllably synthesized by adjusting the Pt/Pd ratios in the sequential reduction method. The Pd@Pt_{1L} NPs are obtained at a Pt/Pd ratio of 0.25/1 when 5.6 nm Pd NPs are used as seeds for deposition of Pt. The catalytic performances of p-CNB hydrogenation with H₂ over Pd@Pt core-shell NPs are dependent on the thickness of Pt shells. At Pt/Pd ratios of 0.25/1 and higher, the Pd@Pt core-shell NPs show better catalytic performance in p-CNB hydrogenation than Pd, Pt, and the physical mixtures of Pd and Pt. The Pd@Pt_{1L} NPs demonstrate superior structural stability either during cycle to cycle p-CNB hydrogenation reactions under mild conditions or during the catalytic reactions under high temperatures and high H₂ pressures. The unexpected superior structural stability and corresponding catalytic stability of Pd@Pt NPs with one atomic Pt layer are ascribed to the strong binding between Pt surfaces and reactants/products during catalytic reactions, where the reactant and product molecules stabilize the Pt surfaces by strong coordination. The superior catalytic performance over Pd@Pt NPs is possibly due to the core-shell interaction. The findings in this study should be helpful in the design of kinetically stabilized core@shell bimetallic NPs with thin shells and could be extended to other catalytic reactions.

■ ASSOCIATED CONTENT

§ Supporting Information

The following file is available free of charge on the ACS Publications website at DOI: 10.1021/cs501612g.

Additional information on binding energies, catalytic performance, phase mapping, characterization data, and calculations ([PDF](#))

■ AUTHOR INFORMATION

Corresponding Authors

*L.C.: e-mail, chenliang@nimte.ac.cn.

*B.E.: e-mail, eichhorn@umd.edu.

*S.Z.: fax, (+86) 574-86685043; e-mail, zhoush@nimte.ac.cn.

Author Contributions

[†]These authors (P.Z. and Y.H.) are equal contributors.

Notes

The authors declare no competing financial interest.

■ ACKNOWLEDGMENTS

S.Z. thanks the Ministry of Science and Technology of China (Grant No. 2012DFA40550) for financial support. H.Y. thanks the Ningbo Municipal Natural Science Foundation (Grant No. 2013A610038) for financial support. L. C. thanks the National Key Basis Research Program of China (Grant No. 2013CB934800).

REFERENCES

- (1) Scott, R. W. J.; Datye, A. K.; Crooks, R. M. *J. Am. Chem. Soc.* **2003**, *125*, 3708–3709.
- (2) He, J. H.; Ichinose, I.; Kunitake, T.; Nakao, A.; Shiraishi, Y.; Toshima, N. *J. Am. Chem. Soc.* **2003**, *125*, 11034–11040.
- (3) Dhital, R. N.; Karnonsatikul, C.; Somsook, E.; Bobuatong, K.; Ehara, M.; Karanjit, S.; Sakurai, H. *J. Am. Chem. Soc.* **2012**, *134*, 20250–20253.
- (4) Scott, R. W. J.; Wilson, O. M.; Oh, S. K.; Kenik, E. A.; Crooks, R. M. *J. Am. Chem. Soc.* **2004**, *126*, 15583–15591.
- (5) Wilson, O. M.; Scott, R. W. J.; Garcia-Martinez, J. C.; Crooks, R. M. *J. Am. Chem. Soc.* **2005**, *127*, 1015–1024.
- (6) Scott, R. W. J.; Sivadinarayana, C.; Wilson, O. M.; Yan, Z.; Goodman, D. W.; Crooks, R. M. *J. Am. Chem. Soc.* **2005**, *127*, 1380–1381.
- (7) Kakade, B. A.; Tamaki, T.; Ohashi, H.; Yamaguchi, T. *J. Phys. Chem. C* **2012**, *116*, 7464–7470.
- (8) Cho, Y. H.; Cho, Y. H.; Lim, J. W.; Park, H. Y.; Jung, N.; Ahn, M.; Choe, H.; Sung, Y. E. *Int. J. Hydrogen Energy* **2012**, *37*, 5884–5890.
- (9) Basu, D.; Basu, S. *Int. J. Hydrogen Energy* **2012**, *37*, 4678–4684.
- (10) Slanac, D. A.; Li, L.; Mayoral, A.; Yacaman, M. J.; Manthiram, A.; Stevenson, K. J.; Johnston, K. P. *Electrochim. Acta* **2012**, *64*, 35–45.
- (11) Liu, Y.; Chi, M. F.; Mazumder, V.; More, K. L.; Soled, S.; Henao, J. D.; Sun, S. H. *Chem. Mater.* **2011**, *23*, 4199–4203.
- (12) Mougenot, M.; Caillard, A.; Brault, P.; Baranton, S.; Coutanceau, C. *Int. J. Hydrogen Energy* **2011**, *36*, 8429–8434.
- (13) Liu, L.; Samjeske, G.; Nagamatsu, S.; Sekizawa, O.; Nagasawa, K.; Takao, S.; Imaizumi, Y.; Yamamoto, T.; Uruga, T.; Iwasawa, Y. *J. Phys. Chem. C* **2012**, *116*, 23453–23464.
- (14) Kakade, B. A.; Wang, H. L.; Tamaki, T.; Ohashi, H.; Yamaguchi, T. *RSC Adv.* **2013**, *3*, 10487–10496.
- (15) Li, C. L.; Yamauchi, Y. *Chem. Eur. J.* **2014**, *20*, 729–733.
- (16) Agnus, Y.; Louis, R.; Weiss, R. *J. Am. Chem. Soc.* **1979**, *101*, 3381–3384.
- (17) Bonomi, R.; Selvestrel, F.; Lombardo, V.; Sissi, C.; Polizzi, S.; Mancin, F.; Tonellato, U.; Scrimin, P. *J. Am. Chem. Soc.* **2008**, *130*, 15744–15745.
- (18) Daniel, M. C.; Astruc, D. *Chem. Rev.* **2004**, *104*, 293–346.
- (19) Ghosh Chaudhuri, R.; Paria, S. *Chem. Rev.* **2012**, *112*, 2373–2433.
- (20) Eryazici, I.; Moorefield, C. N.; Newkome, G. R. *Chem. Rev.* **2008**, *108*, 1834–1895.
- (21) Kobayashi, H.; Yamauchi, M.; Kitagawa, H.; Kubota, Y.; Kato, K.; Takata, M. *J. Am. Chem. Soc.* **2008**, *130*, 1818–1819.
- (22) Xie, S.; Choi, S.-I.; Lu, N.; Roling, L. T.; Herron, J. A.; Zhang, L.; Park, J.; Wang, J.; Kim, M. J.; Xie, Z.; Mavrikakis, M.; Xia, Y. *Nano Lett.* **2014**, *14*, 3570–3576.
- (23) Toshima, N.; Shiraishi, Y.; Shiotsuki, A.; Ikenaga, D.; Wang, Y. *Eur. Phys. J. D* **2001**, *16*, 209–212.
- (24) Wang, Y.; Toshima, N. *J. Phys. Chem. B* **1997**, *101*, 5301–5306.
- (25) Alayoglu, S.; Eichhorn, B. *J. Am. Chem. Soc.* **2008**, *130*, 17479–17486.
- (26) Chen, Y. M.; Liang, Z. X.; Yang, F.; Liu, Y. W.; Chen, S. L. *J. Phys. Chem. C* **2011**, *115*, 24073–24079.
- (27) Cantane, D. A.; Oliveira, F. E. R.; Santos, S. F.; Lima, F. H. B. *Appl. Catal., B* **2013**, *136*, 351–360.
- (28) Kobayashi, H.; Yamauchi, M.; Kitagawa, H.; Kubota, Y.; Kato, K.; Takata, M. *J. Am. Chem. Soc.* **2010**, *132*, 5576–5577.
- (29) Kim, Y.; Noh, Y.; Lim, E. J.; Lee, S.; Choi, S. M.; Kim, W. B. *J. Mater. Chem. A* **2014**, *2*, 6976–6986.
- (30) Yamakawa, S.; Asahi, R.; Koyama, T. *Surf. Sci.* **2014**, *622*, 65–70.
- (31) Bertolini, J. C. *Appl. Catal. A: Gen.* **2000**, *191*, 15–21.
- (32) Deng, H. Q.; Hu, W. Y.; Shu, X. L.; Zhao, L. H.; Zhang, B. W. *Surf. Sci.* **2002**, *517*, 177–185.
- (33) Greeley, J.; Mavrikakis, M. *Nat. Mater.* **2004**, *3*, 810–815.
- (34) West, P. S.; Johnston, R. L.; Barcaro, G.; Fortunelli, A. *Eur. Phys. J. D* **2013**, *67*, 165–174.
- (35) Toshima, N.; Yonezawa, T.; Kushihashi, K. *J. Chem. Soc., Faraday Trans.* **1993**, *89*, 2537–2543.
- (36) Anderson, R. M.; Zhang, L.; Loussaert, J. A.; Frenkel, A. I.; Henkelman, G.; Crooks, R. M. *ACS Nano* **2013**, *7*, 9345–9353.
- (37) Jin, M.; Zhang, H.; Xie, Z.; Xia, Y. *Energy. Environ. Sci.* **2012**, *5*, 6352–6357.
- (38) Doniach, S.; Sunjic, M. *J. Phys. C Solid State Phys.* **1970**, *3*, 285–291.
- (39) Burn, M.; Berthet, A.; Bertolini, J. C. *J. Electron Spectrosc. Relat. Phenom.* **1999**, *104*, 55–60.
- (40) Bera, P.; Priolkar, K. R.; Gayen, A.; Sarode, P. R.; Hegde, M. S.; Emura, S.; Kumashiro, R.; Jayaram, V.; Subbanna, G. N. *Chem. Mater.* **2003**, *15*, 2049–2060.
- (41) Scire, S.; Crisafulli, C.; Maggiore, R.; Minico, S.; Galvagno, S. *Appl. Surf. Sci.* **1996**, *93*, 309–316.
- (42) Collins, S. E.; Baltanas, M. A.; Bonivardi, A. L. *Appl. Catal. A: Gen.* **2005**, *295*, 126–133.
- (43) Chen, C. S.; Lin, J. H.; Chen, H. W. *Appl. Catal. A: Gen.* **2006**, *298*, 161–167.
- (44) Lear, T.; Marshall, R.; Lopez-Sanchez, J. A.; Jackson, S. D.; Klapotke, T. M.; Baumer, M.; Rupprechter, G.; Freund, H. J.; Lennon, D. *J. Chem. Phys.* **2005**, *123*, 174706–174719.
- (45) Greenler, R. G.; Burch, K. D.; Kretzschmar, K.; Klausner, R.; Bradshaw, A. M.; Hayden, B. E. *Surf. Sci.* **1985**, *152*, 338–345.
- (46) Moses-DeBusk, M.; Yoon, M.; Allard, L. F.; Mullins, D. R.; Wu, Z. L.; Yang, X. F.; Veith, G.; Stocks, G. M.; Narula, C. K. *J. Am. Chem. Soc.* **2013**, *135*, 12634–12645.
- (47) Haaland, D. M.; Williams, F. L. *J. Catal.* **1982**, *76*, 450–465.
- (48) Cardenas-Lizana, F.; Hao, Y. F.; Crespo-Quesada, M.; Yuranov, I.; Wang, X. D.; Keane, M. A.; Kiwi-Minsker, L. *ACS Catal.* **2013**, *3*, 1386–1396.
- (49) Wang, X.; Perret, N.; Delgado, J. J.; Blanco, G.; Chen, X.; Olmos, C. M.; Bernal, S.; Keane, M. A. *J. Phys. Chem. C* **2013**, *117*, 994–1005.
- (50) Liu, H.; Deng, J.; Li, W. *Catal. Lett.* **2010**, *137*, 261–266.
- (51) Rode, C. V.; Vaidya, M. J.; Chaudhari, R. V. *Org. Process Res. Dev.* **1999**, *3*, 465–470.
- (52) Barcaro, G.; Fortunelli, A.; Polak, M.; Rubinovich, L. *Nano Lett.* **2011**, *11*, 1766–1769.
- (53) Aiken, J. D.; Finke, R. G. *J. Mol. Catal. A: Chem.* **1999**, *145*, 1–44.